Computational study of drag increase due to wall roughness for hypersonic flight

L. Wang
wangliang12@tsinghua.edu.cn

Y. Zhao and S. Fu
School of Aerospace Engineering
Tsinghua University
Beijing
China

ABSTRACT

In this study, a series of numerical experiments are performed on supersonic/hypersonic flows over an adiabatic flat plate with transitionally and fully rough surfaces. The Mach numbers simulated are 4, 5, 6, and 7; the flight heights considered are 20, 24, 28, 32, and 36 km. First, a modified roughness correction is proposed and validated with the measured data for low-speed flat-plate cases. It is verified that for the equivalent sand grain heights in the intermediate and fully rough regimes, there is a good agreement with the semi-empirical formula available in the open literature. Then, this roughness correction is applied to high-speed flow regime to investigate the effects of flight heights and Mach numbers on drag for rough-wall flat-plate cases. It is found that within the roughness measured in real flight, the roughness height change has little effect on drag compared to the variations of both flight heights and Mach numbers. The drag coefficient derivation between rough-wall and smooth-wall conditions, achieves the maximum value of 0.79% for the 60 cases selected.

Keywords: Turbulence modelling; wall roughness; high-speed flow; equivalent sand grain

NOMENCLATURE

C_d	drag coefficient
C_f	skin friction coefficient
C_p	pressure coefficient
h	enthalpy
H	flight height, km
k	turbulent kinetic energy, m^2/s^2
k_r	equivalent sand grain height, mm
k_r^+	dimensionless roughness height, $k_r^+ = k_r u_\tau / \upsilon$
L	flat-plate length, m
M	mach number
Re	reynolds number, 1/m
S	strain rate magnitude, 1/s
T	temperature, K
u_τ	friction velocity, $u_\tau = (\tau_w/\rho)^{0.5}$
y	wall distance, mm
$\Delta C_d^{\%}$	relative rough-wall C_d derivation from the smooth-wall case
Δu	vertical velocity shift of the logarithmic profile
γ_g	specific heat ratio, $\gamma_g = 1.4$
μ	dynamic viscosity, $\mu = \rho \upsilon$
ν	kinetic viscosity, m^2/s
ν_T	eddy viscosity, m^2/s
τ_w	wall shear stress, $\tau_w = \rho \upsilon \, \partial u/\partial y|_w$
ω	specific turbulence dissipation rate

Subscripts

o	reservoir conditions
w	wall
∞	free-stream value

1.0 INTRODUCTION

In high-speed flight, the surfaces on rocket nozzles or re-entry nosecaps are always rough due to ablation. As the roughness height increases, the onset of laminar-turbulent flow transition gradually moves upstream[1,2]. Once the boundary layer becomes turbulent, heat transfer can increase by a factor of 10. Therefore, the accurate and reliable prediction of the effects of surface roughness on fluid flow and heat transfer is critical for the design and optimisation of future space vehicles operating at sustained supersonic and hypersonic speeds. However, compared to the researches of the surface roughness effect on the aerofoils with icing or turbine blades, very few experimental investigations of the corresponding high-speed cases have been completed up to date[3].

There are various approaches to predict flow over rough surfaces. Hierarchically, these approaches involve, in order of descending requirement in computer resource, DNS (direct numerical simulation), LES (large eddy simulation), DEA (discrete element approach) and equivalent sand grain approach. Lu and Liou[4] and Busse and Sandham[5] reviewed the

progress and state of DNS and LES of flow around roughness elements, which is still limited to simple geometries at a research level. The idea of DEA is to modify the mean flow equations to account for blockage effects due to the presence of roughness elements as well as drag and heat flux on the roughness elements. This technique was introduced by Robertson[6] and further refined by Finson[7], Coleman et al[8] and McClain et al[9,10]. However, it is difficult for DEA to be implemented into a general-purpose CFD (Computational Fluid Dynamics) code for they require altering the flow equations. There is no prospect of adequately handling non-uniform roughness effects in the Reynolds-Averaged Navier-Stokes (RANS) environment[11]. The equivalent sand grain approach is thus adopted in the present study because it is the most popular and the only engineering approach.

The concept of equivalent sand grain roughness was introduced by Schlichting[12], to relate any rough surface to the sand grain size that would yield the same drag increase in the fully rough regime. The sand grain height, k_r^+, is introduced as a new parameter in the RANS turbulence model, either with wall functions[13,14] or with near-wall resolution[15-22], to enhance turbulence in the wall region. However, the drag increase is essentially due to pressure forces on the roughness elements, while this approach only increases the frictional drag. Although it is unphysical and its performance depends on the turbulence model selected, the present approach has been widely accepted due to the simplicity to implement in RANS solvers as well as its comparably high efficiency in calculations[11].

In turbulence models with the equivalent sand grain approach, the rough surface is replaced by an effective, smooth surface, on which modified boundary conditions are imposed. For low-Re turbulence models, an effective displacement of the wall distance origin was introduced by Aupoix and Spalart for the SA (Spalart and Allmaras) one equation model[18] and by Durbin et al for the two layer k–ε model[22], respectively. The effective displacement is related to a hydrodynamic roughness length that is used to modify turbulence length scales as well as the boundary condition for turbulent quantities. The similar approach was also proposed to extend the k–ω type models to account for wall roughness. An early example is the Wilcox roughness modification[19]. However, the Wilcox model requires a very fine mesh resolution and is not accurate for transitionally rough walls. The subsequent models by Seo[21] and Knopp et al[15] give satisfactory results with near wall grid spacing similar to that for smooth walls. It is noted that in the aerodynamically smooth regime, the roughness elements are embedded in the viscous sublayer; whereas in the fully rough regime, the drag increase is only due to pressure forces on the roughness elements; the transitionally rough regime is between these two regimes, where both viscous and pressure forces on the roughness elements contribute to the drag. So far, the applications of these roughness modifications have been limited to low-speed flow regime[11].

Furthermore, within the RANS framework, a few recent studies propose roughness-induced transition models. They are based on an empirical correlation for the momentum thickness Reynolds number at which transition starts. The correlation in Stripf et al[23] depends on both k_r^+ and density, while Boyle and Stripf[24] propose a simpler formula that only depends on k_r^+. Elsner and Warzecha[25] introduced the roughness transition correlation by Stripf et al[23] into the γ-$Re_{\theta t}$ transition model proposed by Langtry and Menter[26] for smooth walls, while Dassler et al[27] extended the γ-$Re_{\theta t}$ model to account for wall roughness in a different type. Both of them chose Wilcox's roughness boundary condition[19] for the fully turbulent boundary layer. Similarly, Ge and Durbin[28] considered the wall roughness effect based on their own smooth-wall transition model[29].

Roy and Blottner reviewed and assessed turbulence models for hypersonic flows[30]. It is found that the Menter k–ω SST (Shear Stress Transport) model[31] with compressibility corrections[32,33] preforms the best among a total of 18 one- and two-equation turbulence models. The compressibility corrections have been carefully examined for their effects on a hypersonic validation database. With the use of SST model with the compressibility corrections, the present authors have conducted high-speed simulations with a reasonably wide range of Mach number[2,34-38], such as supersonic and hypersonic flows past cones at small incidences and elliptic cones at zero incidences. The objective of this work is thus to simulate supersonic/hypersonic flows over a flat plate with transitionally and fully rough surface, by using the SST model with advanced compressibility as well as roughness corrections. Particularly, a modified roughness correction is proposed and validated by the present authors.

This article is organised as follows: Section 2 presents the mathematical formulation of the SST turbulence model including the modifications needed to represent the effects of sand-grain roughness as well as flow compressibility; Section 3 gives the numerical details, especially for boundary conditions; the comparison of the predictions with reference values from the literature for model validation is presented in Section 4; while Section 5 includes the numerical results on systematically refined grids to investigate the drag increase due to wall roughness for hypersonic flat-plate flows; the conclusions of this study are summarised in Section 6.

2.0 MATHEMATICAL FORMULATION

2.1 Menter's k–ω SST model

This model requires the solution of transport equations for k and ω:

$$\frac{\partial \rho k}{\partial t} + \frac{\partial}{\partial x_j}\left[\rho u_j k - (\mu + \sigma_k \mu_t)\frac{\partial k}{\partial x_j}\right] = \tau_{ij}S_{ij} - \beta^* \rho k \omega \qquad \dots(1)$$

and

$$\frac{\partial \rho \omega}{\partial t} + \frac{\partial}{\partial x_j}\left[\rho u_j \omega - (\mu + \sigma_\omega \mu_t)\frac{\partial \omega}{\partial x_j}\right] = P_\omega - \beta k \omega^2 + 2(1-F_1)\frac{\rho \sigma_{\omega 2}}{\omega}\frac{\partial k}{\partial x_j}\frac{\partial \omega}{\partial x_j},$$
$$\dots(2)$$

where S is the mean strain rate, and F_1 is a blending function expressed as

$$F_1 = \tanh\left\{\left\{\min\left[\max\left(\frac{\sqrt{k}}{0.09\omega d}, \frac{500\mu}{\rho d^2 \omega}\right), \frac{4\rho\sigma_{\omega 2}k}{CD_{k\omega}d^2}\right]\right\}^4\right\}, \qquad \dots(3)$$

with

$$CD_{k\omega} = \max\left(\frac{2\rho\sigma_{\omega 2}}{\omega}\frac{\partial k}{\partial x_j}\frac{\partial \omega}{\partial x_j}, 10^{-20}\right), \qquad \dots(4)$$

and the model constants[31] depend on F_1. The eddy-viscosity μ_T is calculated from

$$\mu_t = \min \left(\frac{\rho k}{\omega}, \frac{\rho a_1 k}{\Omega F_2} \right), \qquad \dots (5)$$

where $a_1 = 0.31$, and F_2 is also a blending function:

$$F_2 = \tanh \left\{ \left[\max \left(\frac{2\sqrt{k}}{0.09\omega d}, \frac{500\mu}{\rho d^2 \omega} \right) \right]^2 \right\} \qquad \dots (6)$$

2.2 Velocity shift by wall roughness

A key parameter to characterise the roughness effects is the dimensionless roughness height

$$k_r^+ = k_r u_\tau / \nu, \qquad \dots (7)$$

where k_r is the equivalent sand grain height, $u_\tau = (\tau_w/\rho)^{0.5}$ the friction velocity based upon the wall shear stress, $\tau_w = \rho\nu \, \partial u/\partial y|_w$, the density ρ and the viscosity ν. Nikuradse proposed $k_r^+ = 3.5$ and $k_r^+ = 68$ as the limits of the transitional roughness regime[39].

Near the wall, the flow is highly perturbed by the presence of the roughness elements. Nikuradse[39] pointed out that, above the roughness sublayer, the logarithmic law is preserved but shifted. The velocity profile can be described by

$$\frac{u}{u_\tau} = \frac{1}{\kappa} \ln \left(\frac{y}{k_r} \right) + B, \qquad \dots (8)$$

where κ of 0.41 is Karman constant, B is of 8 under fully rough conditions ($k_r^+ > 68$), while for hydrodynamically smooth walls ($k_r^+ < 3.5$), the classical log-law

$$\frac{u}{u_\tau} = \frac{1}{\kappa} \ln \left(\frac{yu_\tau}{\nu} \right) + 5.1 \qquad \dots (9)$$

is formally recovered by setting $B = \kappa^{-1} \ln (k_r^+) + 5.1$. Then, if Δu, the vertical shift of the logarithmic profile, is defined in terms of u by

$$\frac{u}{u_\tau} = \frac{1}{\kappa} \ln \left(\frac{y + \Delta u}{\Delta u} \right) \qquad \dots (10)$$

Equations (8) and (10) give

$$\frac{y}{k_r} e^{B\kappa} = \frac{y + \Delta u}{\Delta u} \qquad \dots (11)$$

Using the approximation that $\Delta u/y$ is infinitesimal of higher order, the dimensionless velocity shift can thus be expressed as

$$\Delta u^+ = \frac{\Delta u \cdot u_\tau}{\nu} = e^{-B\kappa} \frac{k_r \cdot u_\tau}{\nu} = e^{-B\kappa} k_r^+ \qquad \dots (12)$$

2.3 Roughness corrections

In the present approach, the rough surface is replaced by an effective, smooth surface, on which new boundary conditions are imposed. Under fully rough conditions, the log-layer solution $k = u_\tau^2/C_\mu^{0.5}$, with $C_\mu = 0.09$, extends to the effective wall origin, where the log-layer eddy viscosity $\nu_T = u_\tau \kappa \, (y + \Delta u)$ reduces to $\nu_T = u_\tau \, \kappa \Delta u$. From the definition $\nu_T = k/\omega$, the boundary condition for ω should be

$$\omega = \frac{u_\tau}{C_\mu^{0.5} \kappa \Delta u} \qquad \qquad \dots (13)$$

Generally, the present work adopts the ω boundary condition proposed by Knopp et al[15], as represented as

$$\omega_w = \min \left(\frac{u_\tau}{C_\mu^{0.5} \kappa \Delta u \phi_{r2}}, \, \frac{800\nu}{y_1} \right), \qquad \qquad \dots (14)$$

where Δu equals to 0.03 k_r according to Formula (12), y_1 is the grid point next to the wall and

$$\phi_{r2} = \min \left[1 \, , \, \left(\frac{k_r^+}{30} \right)^{2/3} \right] \min \left[1 \, , \, \left(\frac{k_r^+}{45} \right)^{1/4} \right] \min \left[1 \, , \, \left(\frac{k_r^+}{60} \right)^{1/4} \right] \qquad \qquad \dots (15)$$

Under transitionally rough conditions, Knopp et al[15] use a linear blending function

$$k_w = \frac{u_\tau^2}{C_\mu^{0.5}} \min \left(1 \, \frac{k_r^+}{90} \right) \qquad \qquad \dots (16)$$

for the k boundary condition. However, due to its first derivative discontinuity, we found that the use of Formula (16) might lead to sudden jumps of the skin friction distribution in streamwise direction. Therefore, the present authors propose a more continuous representation as expressed as

$$k_w = \frac{u_\tau^2}{C_\mu^{0.5}} \left[tanh \left(\frac{k_r^+}{60} \right) \right]^2 \qquad \qquad \dots (17)$$

2.4 Compressibility corrections

The above Menter's k–ω SST model was developed mostly for incompressible flows. To account for compressibility effects, it is necessary to re-examine the Favre-averaged equation for the turbulent kinetic energy k which can be written as

$$\bar{\rho} \frac{Dk}{Dt} = \bar{\rho} P_k - \bar{\rho} \varepsilon_s - \bar{\rho} \varepsilon_d + T_k + \overline{p'd''} + M, \qquad \qquad \dots (18)$$

where the terms on the right-hand side are the production term of turbulent kinetic energy $\bar{\rho} P_k$, the solenoidal (incompressible) dissipation $\bar{\rho} \varepsilon_s$, the dilatation (compressible) dissipation $\bar{\rho} \varepsilon_d$, the turbulent transport term T_k, the pressure-dilatation term $\overline{p'd''}$, and the mass flux variation M. The dilatation-dissipation and pressure-dilatation terms appear explicitly in k equation

and directly affect the turbulence energetics. Here, we adopt the dilatation-dissipation model proposed by Sarkar et al[32] as

$$\varepsilon_d = 0.6 M_t^2 \varepsilon_s \qquad \ldots (19)$$

The term M_t is the turbulent Mach number defined by $M_t = (2k)^{0.5}/a$, a being the speed of sound. The pressure-dilatation model proposed by Sarkar[33] reads

$$\overline{p'd''} = 0.15 \bar{\rho} M_t^2 \varepsilon_s - 0.2 \bar{\rho} M_t P_k \qquad \ldots (20)$$

In all, the SST model equations with compressibility corrections can be expressed as:

$$\frac{\partial (\bar{\rho}k)}{\partial t} + \frac{\partial}{\partial x_j} \left[\bar{\rho} \tilde{u}_j k - (\mu + \sigma_k \mu_t) \frac{\partial k}{\partial x_j} \right] = \bar{\rho} \tilde{\tau}_{ij} \tilde{S}_{ij} (1 - 0.2 \bar{\rho} M_t) - \beta^* \bar{\rho} k \omega \left(1 + 0.75 M_t^2 \right)$$
$$\ldots (21)$$

and

$$\frac{\partial \bar{\rho} \omega}{\partial t} + \frac{\partial}{\partial x_j} \left[\bar{\rho} \tilde{u}_j \omega - (\mu + \sigma_\omega \mu_t) \frac{\partial \omega}{\partial x_j} \right]$$
$$= P_\omega - \beta \bar{\rho} k \omega^2 \left(1 - 0.15 M_t^2 \right) + 2 \left(1 - F_1 \right) \frac{\bar{\rho} \sigma_{\omega 2}}{\omega} \frac{\partial k}{\partial x_j} \frac{\partial \omega}{\partial x_j} \qquad \ldots (22)$$

3.0 NUMERICS

All of the simulations presented here are performed using an in-house code where the three-dimensional compressible Navier-Stokes equations are solved by using Roe's implicit, finite volume, upwind algorithm. By means of the monotone upstream-cantered schemes for conservation laws interpolation of the primitive variables, the quantity in the inviscid fluxes is obtained. The viscous flux terms are calculated by a second-order central difference.

Although the proposal described in Section 2 adopts simple Dirichlet boundary conditions, it depends on the friction velocity u_τ. Its determination requires the numerical evaluation of the normal derivative $\partial / \partial y$ of the tangential velocity component, u_t, at the wall. u_τ is calculated with second-order approximation:

$$u_\tau \simeq \sqrt{\nu \frac{2u_{t,2} - 0.5u_{t,3}}{2y_2 - 0.5y_3}} \qquad \ldots (23)$$

The subscripts 2 and 3 stand for the first two grid nodes away from the wall and $u_{t,1} = y_1 = 0$.

For all test case geometries, gird independence has been achieved. The primarily created "baseline grid" is coarsened and refined in each direction by increasing and decreasing the number of grid points by a factor of 2, respectively. Figure 1 shows the computational domain and mesh for the Ligrani and Moffat flat-plate case[40]. The grid node distribution in the longitudinal (x) direction was non-uniform with clustering of nodes near the leading and trailing edge of the plate using one or two-sided stretching functions by Vinokur[41]. In all the grids, 3/4 of the nodes in the longitudinal direction are located on the plate and 1/4 are
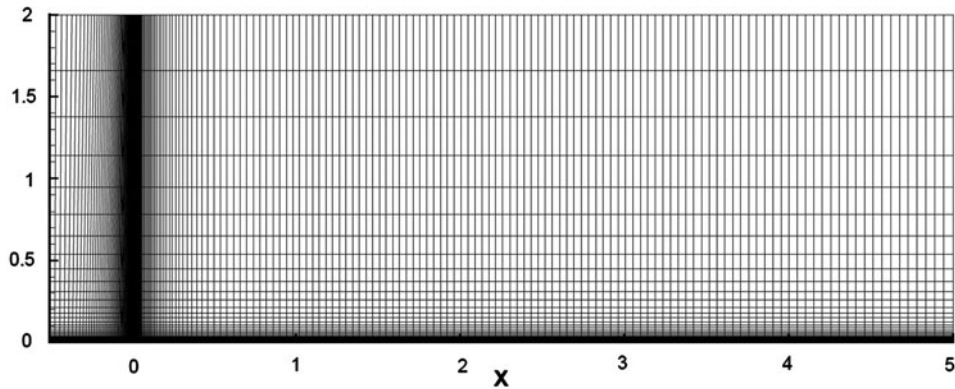
Figure 1. The computational domain and baseline mesh for the Ligrani & Moffat flat-plate case[40].

located upstream of the plate. The number of grid nodes in the longitudinal direction is fixed for the different Reynolds numbers.

In the wall-normal (y) direction, the number of grid nodes depends on the Reynolds number and the near-wall grid line distances. Especially, the grids for the direct application of the no-slip condition are obtained from a one-sided stretching function using different values of the stretching parameter per Reynolds number. For all cases, the first cell y^+ value is of 0.3 with 100 nodes inside the boundary layer. The investigation by Knopp et al[15] led to the choice of these values.

In all cases, steady-state solutions have been obtained on both baseline and refined meshes, which show negligible difference and are therefore judged to be mesh independent. All cases are run to full convergence, determined based on a drop in residuals of typically five orders of magnitude, as well as a flattening of all residuals indicating that machine accuracy has been reached.

4.0 MODEL VALIDATION

The new roughness proposal has been validated for a reasonably wide range of rough-wall cases involving incompressible turbulent flows past flat plates and pipes under zero pressure gradients (PG). The test cases used by Knopp et al are adopted here to ensure that the present modification either improves or doesn't contaminate their original model. Results labelled as "DLR" correspond to those predictions using the roughness correction, Formula (16), proposed by Knopp et al[15]. Those of the present model, Formula (17), are labelled "New" or not labelled. It is noted that the curvature effect is neglected here and will be considered in further works.

4.1 Experiments by Ligrani and Moffat[40]

The test case by Ligrani and Moffat[40] is a flat-plate turbulent boundary layer flow over spherical roughness elements. The flat plate length $L = 5$ m, the kinetic viscosity $v = 1.5$E-5 m^2/s. The roughness height is held constant, with the corresponding equivalent sand grain roughness size k_r of 0.79 mm, as confirmed in an earlier study using fully rough velocity-profiles information[40]. By altering the free-stream velocity, transitionally rough conditions are obtained, as listed in Table 1.

Table 1
Flow conditions in the experiment by Ligrani and Moffat[40]. The values for k_r^+
are measured at $x/L = 0.356$

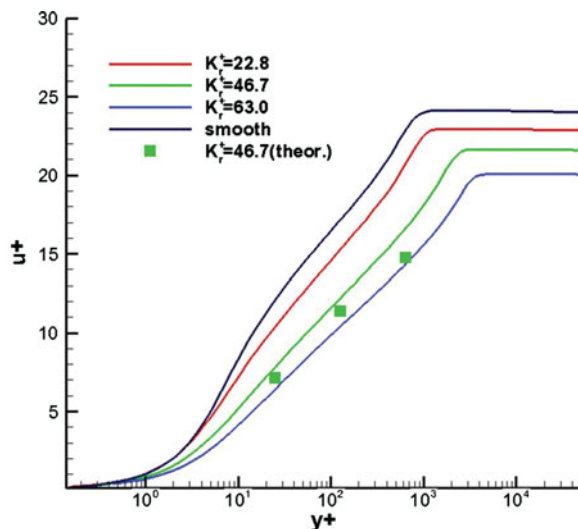|	Case 1	Case 2	Case 3
U_∞ (m/s)	10.1	20.4	26.8
k_r (mm)	0.79	0.79	0.79
k_r^+	22.8	46.7	63.0

Figure 2. (Colour online) Calculated velocity profiles at $x/L = 0.356$, for different dimensionless roughness heights measured at $x/L = 1$.

The predicted velocity profiles in the logarithmic region, as shown in Fig. 2, give good agreement with the theoretical relation, Equation (8), in transitionally rough conditions. It is also seen that with the increase of dimensionless roughness heights, the velocity shift of the logarithmic profile increases. Figure 3 shows the computed skin friction coefficient, C_f, with comparison to experimental data. It indicates that compared to DLR results, ours are closer to the measurements. Note that the uncertainty regarding the experimental data for C_f is about $\pm 10\%$[40]. For this case, the new proposal can achieve reasonable results for both C_f and Δu, which was thought to be difficult for the k–ω type models with roughness corrections[24].

4.2 Experiments by Nikuradse[39]

Here we consider the experiments by Nikuradse[39] for fully developed flows in pipes of various roughness heights. Tables 2 and 3 provide a summary of the parameter variations for high and medium Re (Reynolds number) regimes, respectively. For R/k_r larger than 252 in Table 2 as well as R/k_r larger than 30.6 in Table 3, transitional roughness values can be observed.

The tables also compare the present and DLR predictions for the roughness Reynolds number k_r^+, at $x/L = 1$, with the experimental data. It is noted that the prediction accuracy of

Table 2
Overview of flow parameters at high Reynolds numbers in the Nikuradse experiment[39]. _R_ denotes the pipe radius

_R/k_r_	_Re_	k_r^+ **New**	k_r^+ **DLR**	k_r^+ **Exp.**
15	4.30E5	1204.63	1205.81	1230.27
30.6	6.38E5	795.56	791.26	805.38
60	6.77E5	365.68	365.24	369.83
126	9.60E5	222.25	223.13	229.61
252	6.24E5	63.21	62.17	66.98
507	5.07E5	48.42	47.95	48.53

Table 3
Overview of flow parameters at medium Reynolds numbers in the Nikuradse experiment[39]. _R_ denotes the pipe radius

_R/k_r_	_Re_	k_r^+ **New**	k_r^+ **DLR**	k_r^+ **Exp.**
15	4.30 E4	118.9	119.08	124.45
30.6	4.30 E4	50.81	50.76	52.48
60	7.00 E4	36.55	35.12	37.49
126	5.05 E4	10.96	10.85	11.09
252	5.10 E4	5.33	5.30	5.34
507	4.90 E4	2.53	2.52	2.5
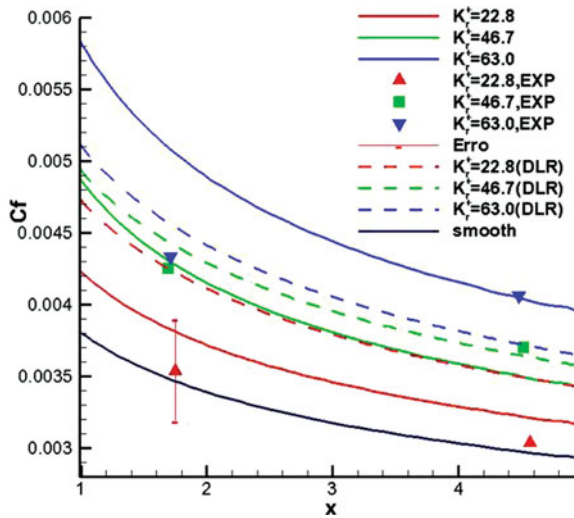
Figure 3. (Colour online) Skin friction (Cf) distributions predicted by the present and the DLR15 models, with comparison to experimental data[40].
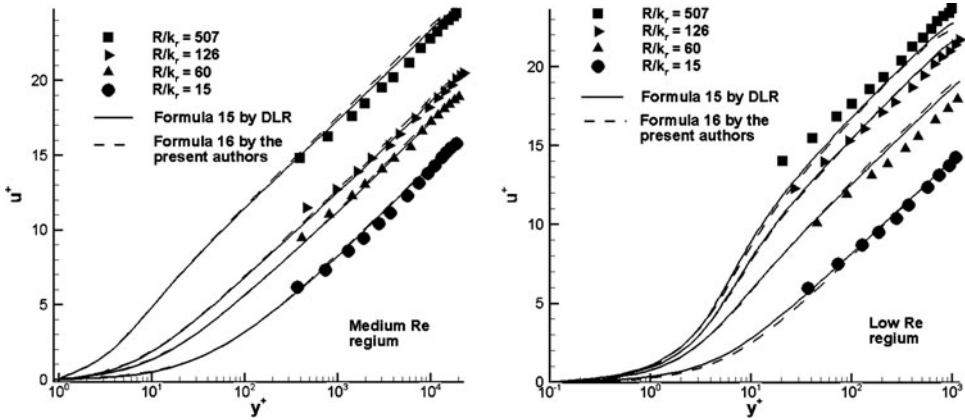
Figure 4. Velocity profiles at medium (left) and low (right) *Re*, predicted by the present and the DLR15 models, with comparison to experimental data[39].
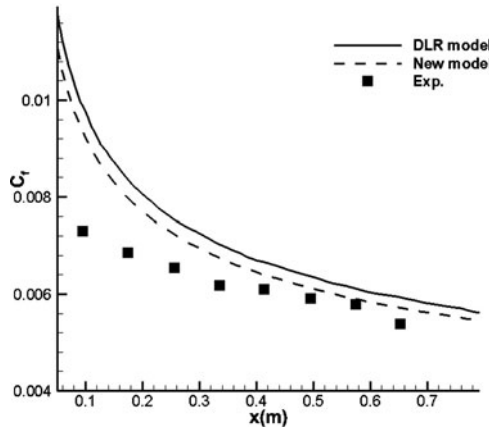

Figure 5. Skin friction (C_f) distributions predicted by the present and the DLR[15] models, with comparison to experimental data[42].

C_f directly depends on the agreement in k_r^+. Good agreement is achieved between calculations and measurements for all the cases. Figure 4 depicts the predicted velocity profiles in the logarithmic region. It is seen that the predicted shift of the log-law matches the measurements fairly well, except for $R/k_r = 507$ at medium *Re* and $R/k_r = 60$ at low *Re*. Nevertheless, the new model gives almost identical predictions with the DLR results.

4.3 Experiment by Blanchard[42]

Blanchard[42] measured zero pressure gradient flow over a rough surface with the equivalent sand grain roughness of 0.85 mm. With reference to the work by Knopp et al[15], the inflow velocity is set to 45 m/s and the reference length $L = 0.8$ m. Figure 5 shows the computed skin friction coefficient, C_f, with comparison to experimental data. It is seen that although there are some gaps between calculations and measurements, the consistent distribution trends.
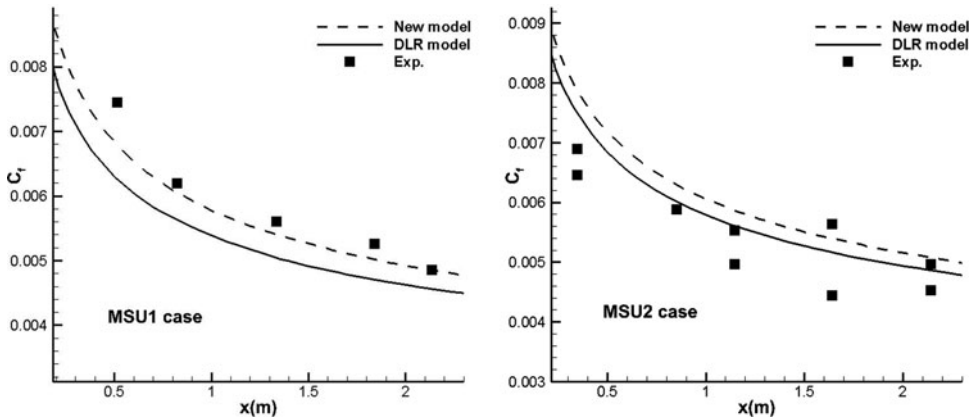
Figure 6. Skin friction (C_f) distributions For both MSU1 and MSU2 cases predicted by the present and the DLR[15] models, with comparison to experimental data[43,44].

4.4 Experiments by Hosni et al[43, 44]

Hosni et al[43,44] experimentally studied the turbulent boundary layer flow over a rough surface of length $L = 2.4$ m composed of hemispheres of diameter $l_0 = 1.27$ mm. The equivalent sand grain roughness is of 1.09 mm. The investigation by Knopp et al[15] led to the choice of this value. The test case MSU1 with inflow velocity of 12 m/s, gives the transitional roughness value, $k_r^+ = 40$, at $x = 2$ m, while the case MSU2 with inflow velocity of 58 m/s, shows the fully rough condition, $k_r^+ = 200$, at $x = 2$ m.

Figure 6 depicts the predicted skin friction coefficient, C_f, with comparison to measurements. For both MSU1 and MSU2 cases, the present and the DLR models give similar C_f distributions. It is noted that for both cases the uncertainty in C_f is estimated to be 10%-12%[43,44].

5.0 RESULTS OF SUPERSONIC/HYPERSONIC FLAT-PLATE FLOW CASES

In this section, our validated method is applied to the supersonic/hypersonic flow past a flat plate with transitionally and fully rough surfaces. The flow conditions considered here refer to the typical atmospheric flight conditions with several flight height levels as well as Mach numbers. At first, we investigate the roughness effect on drag. Then, the effects of flight heights and Mach numbers on drag are studied within the roughness heights measured in real flight. The adiabatic wall boundary conditions are imposed here.

5.1 Roughness effect

The numerical experiments are set up with the inflow conditions as $M_\infty = 6$, $H = 26$ km ($Re_\infty = 4.3$ E6/m, $T_\infty = 222.5$ K), 0° angle-of-attack. The roughness heights simulated are 20 µm, 200 µm, 700 µm and 1,000 µm. Within the baseline grid, the streamwise and wall-normal directions are resolved by 241 and 161 points, respectively.

Figure 7 shows the roughness height effect on the computed velocity shift of the logarithmic profile, which is pretty weak compared with the low-speed case. Especially, the velocity profile at $k_r = 20$ µm almost superpose with the one on the smooth wall. Therefore, dimensionless
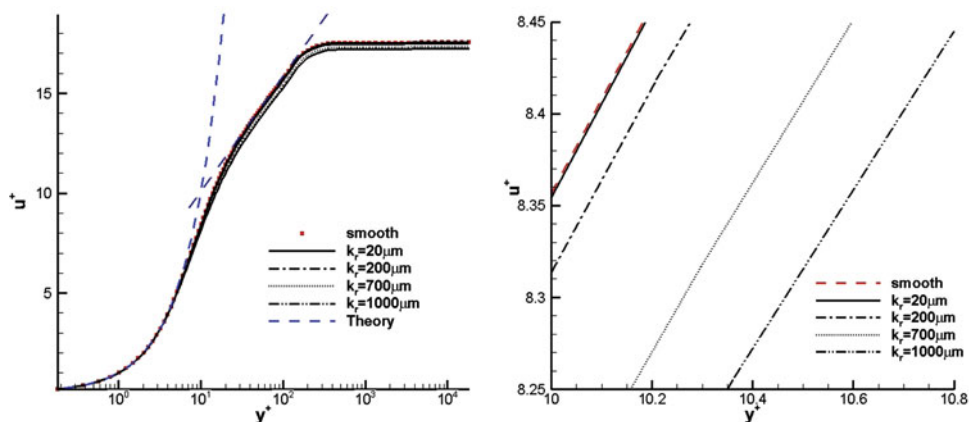
Figure 7. (Colour online) Calculated velocity profiles at $x/L = 0.356$, for different dimensionless roughness heights, the right zooms in the left.
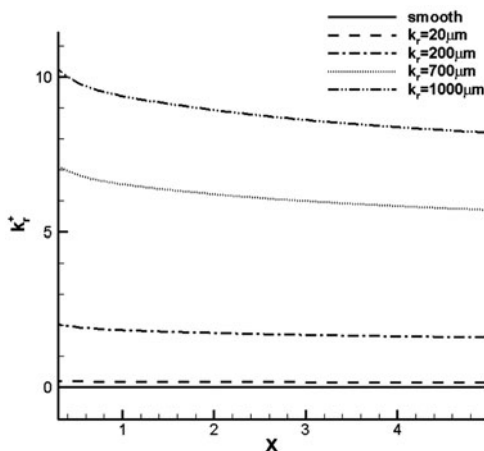

Figure 8. Dimensionless roughness height distributions.

roughness heights need to be calculated, as given in Fig. 8. It is seen that the k_r values of 20 μm and 200 μm correspond to the hydrodynamically smooth walls ($k_r^+ < 3.5$), while the others to the transitional roughness regime ($3.5 < k_r^+ < 68$)as defined by Nikuradse[39] for incompressible channel flows. This can mostly be attributed to the dramatic increase of boundary layer thickness, δ, in hypersonic flows, as estimated by[45]

$$\frac{\delta}{x} \propto \frac{M^2}{\text{Re}_x^2} \qquad \dots (24)$$

The δ variations with different roughness heights (k_r) are given in Table 4. The boundary layer edge is defined as the location where the local total enthalpy achieves 1.005 times the stagnation enthalpy at a certain profile. It verifies that the roughness height is pretty small compared with boundary layer thickness, though its absolute value is already beyond the one

Table 4
Variations of boundary layer thickness (δ) with different roughness heights (k_r) at $x/L = 0.356$

k_r (μm)	0	20	200	700	1,000
δ (mm)	28.93	29.00	29.37	30.19	30.53

Table 5
Variations of the drag coefficient (C_d) as well as the relative rough-wall C_d derivation from the smooth-wall case ($\triangle C_d\%$), with the equivalent sand grain height k_r

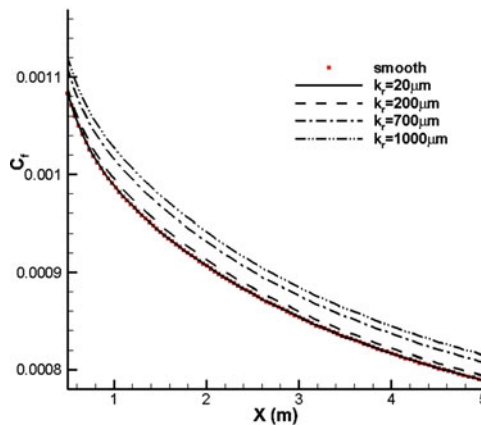| k_r (μm)	C_d	$\triangle C_d\%$
0	0.0014034	0
20	0.0014039	0.036%
200	0.0014164	0.923%
700	0.0014467	3.09%
1,000	0.0014642	4.33%

Figure 9. (Colour online) Predicted skin friction (C_f) distributions for different roughness heights.

for real aircraft surface that is usually smaller than $100\,\mu$m. Moreover, Table 4 indicates that roughness causes additional increase of δ.

Figure 9 depicts the skin friction distribution along the flat plate. It rises with the increase of the roughness height. Since there is no pressure contributed in it, the drag can be integrated from Fig. 9, as given in Table 5. For comparison, it is more reasonable to consider the relative rough-wall drag derivation from the smooth-wall case, as defined as

$$\triangle C_d^{\%} \frac{C_{d,\text{rough}} - C_{d,\text{smooth}}}{C_{d,\text{smooth}}}, \; C_d = \frac{D}{\rho_\infty U_\infty^2 A} \qquad \ldots (25)$$

Table 6
Variations of flow parameters with flight heights at $x = 1$ m, $M_\infty = 4$ and $k_r = 100\,\mu$m

H (km)	20	24	28	32	36
$Re/$m $(\times 10^6)$	7.32	3.83	1.89	1.11	0.581
δ (mm)	7.03	9.71	13.86	18.02	24.9
k_r^+	3.46	1.97	1.06	0.66	0.37

Table 7
Variations of flow parameters with Mach numbers at $x = 1$ m, $H = 36$ km and $k_r = 100\,\mu$m

M	4	5	6	7
$Re/$m $(\times 10^6)$	5.81	7.26	8.72	10.2
δ (mm)	24.9	25.5	26.4	27.1
k_r^+	0.37	0.29	0.23	0.19

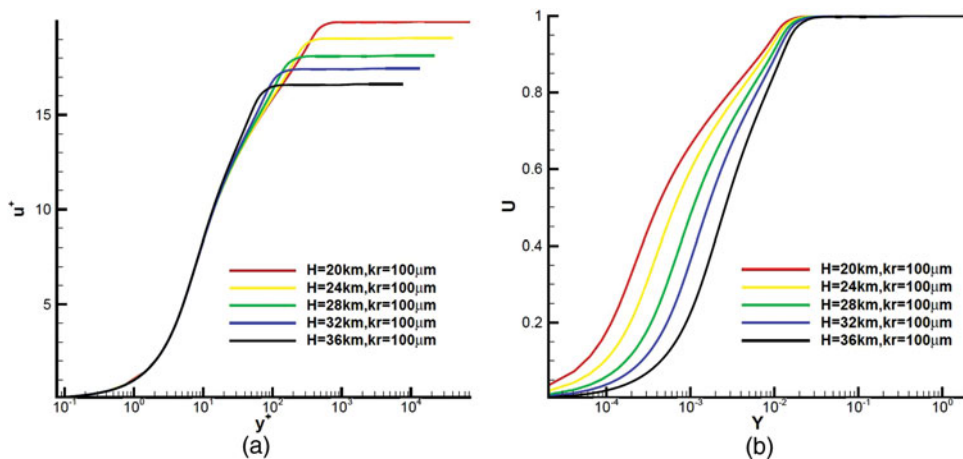Figure 10. (Colour online) Calculated velocity profiles, at $x = 1$ m, for different flight heights. (a) $u^+ = u/u_\tau$, $y^+ = yu_\tau/\nu$; (b) $U = u/U_\infty$, $Y = y/L$. $M = 4$, $k_r = 100\,\mu$m.

Here D is the drag force and A the reference area of 1 m2. It is seen from Table 5 that for the selected inflow conditions, the maximum drag increase of 4.33% is achieved at $k_r = 1,000$ μm. In general, the roughness effect on drag is pretty weak in such hypersonic flat-plate flows.

5.2 Effects of flight heights and Mach numbers

Actually, the roughness height value for real aircraft surface (the nose region excluded) are usually smaller than 100 μm. Therefore, the roughness heights of 20 μm and 200 μm are selected to study the effects of flight heights and Mach numbers on drag with surface roughness. The Mach numbers simulated are 4, 5, 6 and 7; the flight heights considered are 20,
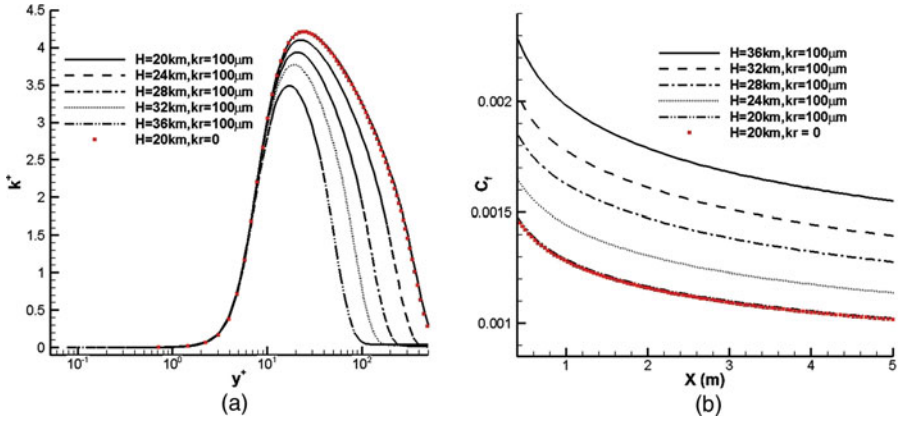
Figure 11. (Colour online) Predicted profiles of dimensionless turbulent kinetic energy (k^+) at $x = 1$ m (a) and skin friction (C_f) distributions (b) for different k_r^+ that correspond to different flight heights at $M_\infty = 4$. $k^+ = 2k/u_\tau^2$.
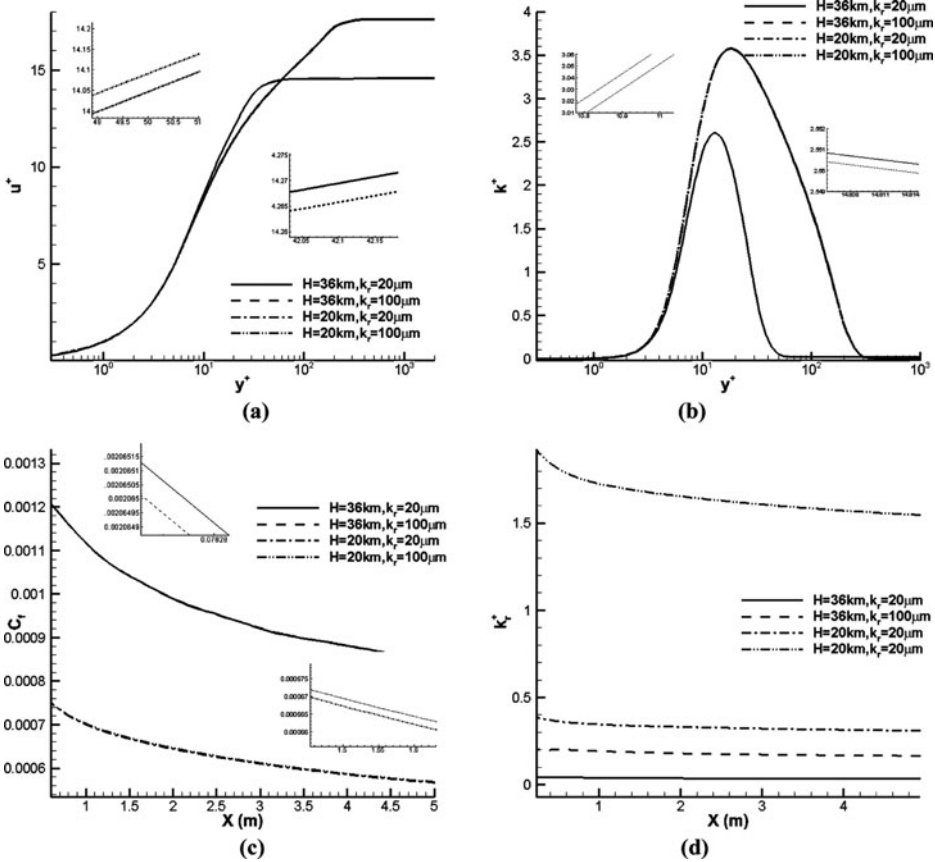

Figure 12. Flow parameter predictions for different flight heights and for different dimensionless roughness heights at $M_\infty = 7$. Profiles of dimensionless velocity (a) and turbulent kinetic energy (b) at $x = 1$ m; skin friction (c) and dimensionless roughness height (d) distributions. $k^+ = 2k/u_\tau^2$.
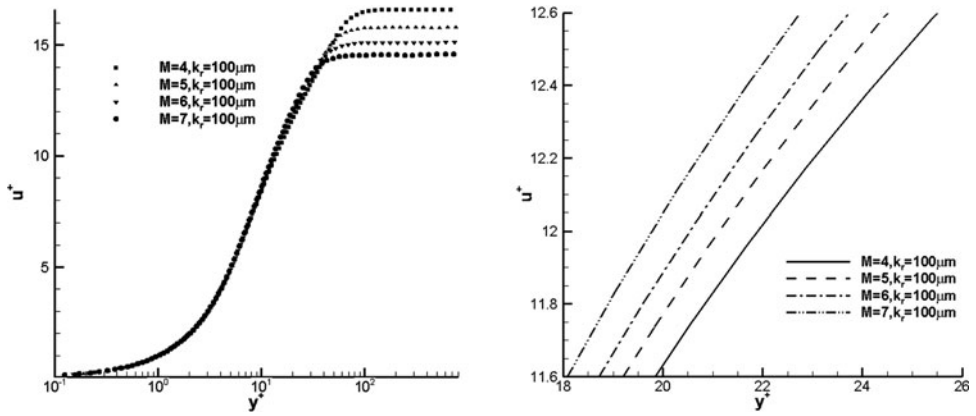
Figure 13. Calculated velocity profiles at $x = 1$ m, for different Mach numbers, the right zooms in the left. $H = 36$ km and $k_r = 100\,\mu$m.
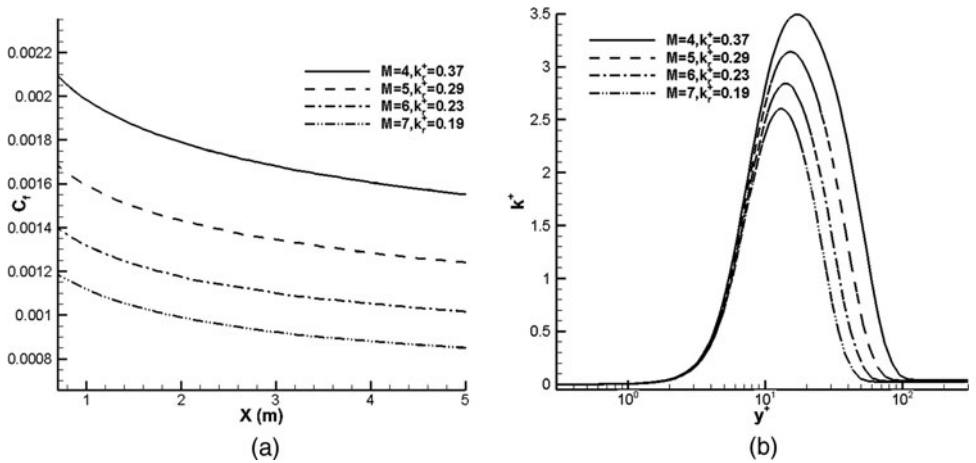

Figure 14. Predicted skin friction (C_f) distributions (a) and profiles of dimensionless turbulent kinetic energy (k^+) at $x = 1$ m (b) for different Mach numbers. $k^+ = 2k/u_\tau^2$, $H = 36$ km and $k_r = 100\,\mu$m.

24, 28, 32 and 36 km. Table 6 shows the unit Reynolds numbers for different flight heights at $M_\infty = 4$. It is seen that with the flight height increase, the air density decrease is more intensive than the dynamic viscosity decrease, resulting in the reduction of unit Reynolds number. The computational meshes are generated corresponding to different Reynolds numbers, as discussed in Section 3.

Figure 10(a) depicts the flight height effect on the computed velocity shift of the logarithmic profile at $x = 1$ m, $M_\infty = 4$ and $k_r = 100\,\mu$m. It is seen that all curves superpose in the near-wall region. If the characteristic length and velocity are chosen as L and U_∞, respectively, the dimensionless velocity profiles (see Fig. 10(b)) shows that with the flight height decrease (*Re* increase), the velocity increases at the same wall distance.

Figure 11(a) plots the near-wall behaviour for turbulent kinetic energy, k, at $x = 1$ m and $M_\infty = 4$. It demonstrates that the new roughness model remedies the near-wall gradient of k appearing for the Wilcox roughness modification[19]. It is seen that the flight height change

Table 8
Variations of drag coefficient (C_d) as well as its relative derivation from the smooth-wall case ($\triangle C_d^{\%}$), with the dimensionless roughness height k_r and the flight height H, at $M_\infty = 4$ (a), 5 (b), 6 (c) and 7 (d)

H (km)	20	24	28	32	36
$C_d \times 10^2$ (smooth)	0.17905	0.20123	0.22815	0.25086	0.28178
$C_d \times 10^2$ ($k_r = 20\,\mu$m)	0.17907	0.20124	0.22823	0.25094	0.28186
$\triangle C_d^{\%}$ ($k_r = 20\,\mu$m)	0.012%	0.004%	0.035%	0.032%	0.025%
$C_d \times 10^2$ ($k_r = 100\,\mu$m)	0.18046	0.20209	0.22856	0.25109	0.28193
$\triangle C_d^{\%}$ ($k_r = 100\,\mu$m)	0.79%	0.43%	0.18%	0.092%	0.050%

(a)

H (km)	20	24	28	32	36
$C_d \times 10^2$ (smooth)	0.14381	0.16156	0.18341	0.20177	0.22734
$C_d \times 10^2$ ($k_r = 20\,\mu$m)	0.14383	0.16162	0.18347	0.20181	0.22740
$\triangle C_d^{\%}$ ($k_r = 20\,\mu$m)	0.016%	0.037%	0.033%	0.019%	0.026%
$C_d \times 10^2$ ($k_r = 100\,\mu$m)	0.14468	0.16210	0.18364	0.20190	0.22744
$\triangle C_d^{\%}$ ($k_r = 100\,\mu$m)	0.60%	0.33%	0.13%	0.066%	0.044%

(b)

H (km)	20	24	28	32	36
$C_d \times 10^2$ (smooth)	0.11829	0.13304	0.15107	0.16651	0.18846
$C_d \times 10^2$ ($k_r = 20\,\mu$m)	0.11831	0.13311	0.15110	0.16654	0.18850
$\triangle C_d^{\%}$ ($k_r = 20\,\mu$m)	0.017%	0.048%	0.020%	0.021%	0.021%
$C_d \times 10^2$ ($k_r = 100\,\mu$m)	0.11888	0.13341	0.15125	0.16660	0.18853
$\triangle C_d^{\%}$ ($k_r = 100\,\mu$m)	0.50%	0.27%	0.12%	0.054%	0.038%

(c)

H (km)	20	24	28	32	36
$C_d \times 10^2$ (smooth)	0.09941	0.11196	0.12743	0.14084	0.16011
$C_d \times 10^2$ ($k_r = 20\,\mu$m)	0.09945	0.11201	0.12746	0.14087	0.16012
$\triangle C_d^{\%}$ ($k_r = 20\,\mu$m)	0.033%	0.036%	0.024%	0.021%	0.006%
$C_d \times 10^2$ ($k_r = 100\,\mu$m)	0.09988	0.11222	0.12757	0.14090	0.16020
$\triangle C_d^{\%}$ ($k_r = 100\,\mu$m)	0.47%	0.23%	0.11%	0.043%	0.052%

(d)

has little effect on k in both viscous sublayer and log-layer regions, which can be attributed to the corresponding small k_r^+ given in Table 6. In contrast, the flight height effect on skin friction distribution is visible, as shown in Fig. 11(b).

Figure 12 compares flow parameters concerned, at $M_\infty = 7$, for different flight heights and for different roughness heights. Duo to k_r^+ inside the hydrodynamically smooth-wall regime for all cases (see Fig. 12(d)), slight difference can be observed between the cases at the same flight height amplitude. With the flight height decrease, significant changes in both velocity and turbulent kinetic energy profiles occur, while the skin friction distributions shift downwards. It can be concluded that the flight height effect is much stronger than the effect of roughness heights considered in the present study.

We then investigate the Mach number effect by maintaining the same flight height. Table 7 shows the flow parameters at $H = 36\,\mathrm{km}$ and $k_r = 100\,\mu\mathrm{m}$. The variation of Mach number is purely due to the change of inflow velocity. It is seen from Figs 13 and 14(a) that with the Mach number increase, the logarithmic profile shifts upwards and the skin friction decreases. Figure 14(b) illustrates that the turbulent kinetic energy trends to zero in the near-wall region, because of the very small k_r^+ for these cases (see Table 7).

By integrating the skin friction distributions along the flat plate, we obtain the drag coefficients C_d for the 60 cases in total, as given in Table 8. It can be concluded that C_d rises with the increase of flight height H (at constant M_∞) while with the increase of Mach number M_∞ (at constant H); the derivation between rough-wall and smooth-wall conditions, $\Delta C_d^{\%}$, achieves the maximum value of 0.79% for the case with $M_\infty = 7$, $H = 36\,\mathrm{km}$ and $k_r = 100\,\mu\mathrm{m}$. It is noted that greater resolution at Mach numbers and flight heights values can be interpolated to those already listed in Table 8.

6.0 CONCLUSION

In this study, a new extension for the SST k–ω turbulence model to account for surface roughness as well as flow compressibility effects has been presented which allows for the simulation of supersonic/hypersonic flows over rough surfaces at the same grid resolution requirements as for smooth walls. The new roughness modification gives slightly improved predictions in skin friction for low-speed cases compared to the roughness extension by Knopp et al[15].

Then, using the current method, aerodynamics of supersonic/hypersonic flows along a flat plate of finite length is investigated numerically with Mach number up to 7 and flight height up to 36 km. It is found that the drag coefficient derivation between rough-wall and smooth-wall conditions, achieves the maximum value of at $k_r = 1{,}000\,\mu\mathrm{m}$, $M_\infty = 6$, $H = 26\,\mathrm{km}$; within the roughness measured in real flight ($k_r < 100\,\mu\mathrm{m}$), the roughness height change has little effect on drag compared to the variations of either flight heights or Mach numbers. This can mostly be attributed to the dramatic increase of boundary layer thickness in hypersonic flows. Hence, the dimensionless roughness height becomes pretty small, approaching the hydrodynamically smooth wall condition.

ACKNOWLEDGEMENTS

REFERENCES

1.   GIANLUCA, E., IACCARINO, S. and SHAQFEH, G. Nonlinear instability of a supersonic boundary layer with two-dimensional roughness, *J Fluid Mechanics*, 2014, **752**, (4), pp 497-520.
2.   FU, S. and WANG, L. RANS modeling of high-speed aerodynamic flow transition with consideration of stability theory, *Progress in Aerospace Sciences*, 2013, **58**, pp 36-59.
3.   BOWERSOX, R. Survey of high-speed rough wall boundary layers, invited presentation, *Proceedings of Proceedings of the 37th AIAA Fluid Dynamics Conference and Exhibit*, 2007.

4. LU, M. and LIOU, W. New two-equation closure for rough-wall turbulent flows using the brinkman equation, *AIAA J*, 2009, **47**, (2), pp 386-398.
5. BUSSE, A. and SANDHAM, N. Parametric forcing approach to rough wall turbulent channel flow, *J Fluid Mechanics*, 2012, **712**, pp 169-202.
6. ROBERTSON, J. Surface Resistance as a Function of the Concentration and Size of Roughness Elements, Ph.D. thesis, State University of Iowa, Ann Arbor, Mich: University Microfilms, Inc., 1961.
7. FINSON, M. A Model for Rough Wall Turbulent Heating and Skin Friction, AIAA Paper, 1982, 82-0199.
8. COLEMAN, H., HODGE, B. and TAYLOR, R. Generalized Roughness Effects on Turbulent Boundary Layer Heat Transfer—A Discrete Element Predictive Approach for Turbulent Flow Over Rough Surfaces, Mississippi State University, Mississippi State Engineering and Industrial Research Station, 1983.
9. McCLAIN, S., HODGE, B. and BONS, J. Predicting skin friction and heat transfer for turbulent flow over real gas turbine surface roughness using the discrete element method, *J Turbomachinery*, 2004, **126**, (2), pp 259-267.
10. McCLAIN, S., COLLINS, S., HODGE, B. and BONS, J. The importance of the mean elevation in predicting skin friction for flow over closely packed surface roughness, *J Fluids Engineering*, 2006, **128**, (3), pp 579-586.
11. AUPOIX, B. Roughness corrections for the k–ω; shear stress transport model: Status and proposals, *J Fluids Engineering*, 2015, **137**, pp 021202-1.
12. SCHLICHTING, H. Experimental Investigation of the Problem of Surface Roughness, NACA Technical Memorandum, NACA Technical Memorandum 823, pp. 1–34, Washington, DC, US, 1937.
13. SUGA, K., CRAFT, T.J. and IACOVIDES, H. An analytical wall-function for turbulent flows and heat transfer over rough walls, *Int J Heat and Fluid Flow*, 2006, **27**, pp 852-66.
14. APSLEY, D. CFD calculation of turbulent flow with arbitrary wall roughness, *Flow, Turbulence and Combustion,* 2007, **78**, (2), pp 153-175.
15. KNOPP, T., EISFELD, B. and CALVO, J.B. A new extension for k–ω; turbulence models to account for wall roughness, *Int J Heat and Fluid Flow*, 2009, **30**, (1), pp 54-65.
16. ECA, L. and HOEKSTRA, M. Numerical aspects of including wall roughness effects in the SST k–ω; eddy-viscosity turbulence model, *Computers & Fluids*, 2011, **40**, (1), pp 299-314.
17. FUHRMAN, D.R., DIXEN, M. and JACOBSEN, N.G. Physically-consistent wall boundary conditions for the k–ω; turbulence model, *J. Hydraulic Research*, 2010, **48**, (6), pp 793-800.
18. AUPOIX, B. and SPALART, P.R. Extensions of the Spalart–Allmaras turbulence model to account for wall roughness, *Int J Heat and Fluid Flow*, 2003, **24**, (4), pp 454-462.
19. WILCOX, D.C. *Turbulence Modeling for CFD*, 3rd ed, 2006, DCW industries La Canada, CA.
20. FOTI, E. and SCANDURA, P. A low Reynolds number k–ε model validated for oscillatory flows over smooth and rough wall, *Coastal Engineering*, 2004, **51**, (2), pp 173-184.
21. SEO, J.M. Closure Modeling and Numerical Simulation for Turbulent Flows: Wall Roughness Model, Realizability, and Turbine Blade Heat Transfer, Ph.D. Thesis, 2004, Flow Physics and Computation Division, Dept. of Mechanical Engineering, Stanford University, Stanford, California, US.
22. DURBIN, P., MEDIC, G., SEO, J.M., EATON, J. and SONG, S. Rough wall modification of two-layer k–ε model, *J. Fluids Engineering*, 2001, **123**, pp 16-21.
23. STRIPF, M., SCHULZ, A., BAUER, H.J. and WITTIG, S. Extended models for transitional rough wall boundary layers with heat transfer, Part I: Model formulations, *J Turbomachinery*, 2009, **131**, p 031016.
24. BOYLE, R. and STRIPF, M. Simplified approach to predicting rough surface transition, *J Turbomachinery*, 2009, **131**, p 41020.
25. ELSNER, W. and WARZECHA, P. Numerical study of transitional rough wall boundary layer, *J Turbomachinery*, 2014, **136**, p 011010.
26. LANGTRY, R. and MENTER, F. Correlation-based transition modelling for unstructured parallelized computational fluid dynamics codes, *AIAA J*, 2009, **47**, pp 2894-2906.
27. DASSLER, P., KOZULOVIĆ, D. and FIALA, A. Modelling of roughness-induced transition using local variables, 5th European Conference on CFD, ECCOMAS CFD, Lisbon, Portugal, June 2010, 14–17.

28. GE, X. and DURBIN, P.A. An intermittency model for predicting roughness induced transition, *Int J Heat and Fluid Flow*, 2015, **54**, (55), pp 55-64.
29. GE, X., AROLLA, S. and DURBIN, P. A bypass transition model based on the intermittency function, *Flow, Turbulence and Combustion*, 2014, **93**, pp 37-61.
30. ROY, C.J. and BLOTTNER, F.G. Review and assessment of turbulence models for hypersonic flows, *Progress in Aerospace Sciences*, 2006, **42**, pp 469-530, Survey Review.
31. MENTER, F.R. Two-equation eddy-viscosity turbulence models for engineering applications, *AIAA J*, 1994, **32**, pp 1598-1605.
32. SARKAR, S., ERLEBACHER, G. and HUSSAINI, M.Y. The analysis and modelling of dilatational terms in compressible turbulence, *J Fluid Mechanics*, 1991, **227**, pp 473-493.
33. SARKAR, S. The stabilizing effect of compressibility in turbulent shear flow, *J Fluid Mech*, 1995, **282**, pp 163-186.
34. WANG, L. and FU, S. Development of an intermittency equation for the modeling of the supersonic/hypersonic boundary layer flow transition, *Flow, Turbulence and Combustion*, 2011, **87**, pp 165-187.
35. WANG, L. and FU, S. Modelling flow transition in hypersonic boundary layer with Reynolds-averaged Navier-Stokes approach, *Science China Physics, Mechanics and Astronomy*, 2009, **52**, (5), pp 768-774.
36. WANG, L., FU, S., CARNARIUS, A., MOCKETT, C. and THIELE, F. A modular RANS approach for modeling laminar-turbulent transition in turbomachinery flows, *Int J Heat and Fluid Flow*, 2012, **34**, pp 62-69.
37. HU, R.Y., WANG, L. and FU, S. Investigation of the coherent structures in flow behind a backward-facing step, *Int J Numerical Methods for Heat*, 2016, **26**, (3/4), pp 1050-1068.
38. WANG, L., XIAO, L. and FU, S. A modular RANS approach for modeling hypersonic flow transition on a scramjet-forebody configuration, *Aerospace Science and Technology*, 2016, **56**, pp 112-124.
39. NIKURADSE, J. Laws of flow in rough pipes. National advisory committee for aeronautics, NACA Technical Memorandum, NACA Technical Memorandum 1292, pp 60–68, Washington, DC, US, 1933.
40. LIGRANI, P.M. and MOFFAT, R.J. Structure of transitionally rough and fully rough turbulent boundary layers, *J Fluid Mechanics*, 1986, **162**, pp 69-98.
41. VINOKUR, M. On one-dimensional stretching functions for finite-difference calculations, *J Computational Physics*, 1983, **50**, pp 215-234.
42. BLANCHARD, A. Analyse Expérimentale et Théorique de la Structure de la Turbulence dúne Couche Limite sur Paroi Rugueuse, Ph.D. thesis, Université de Poitiers U.E.R.-E.N.S.M.A, 1977.
43. HOSNI, M.H., COLEMAN, H.W. and TAYLOR, R.P. Measurements and calculations of rough-wall heat transfer in the turbulent boundary layer, *Int J Heat and Mass Transfer*, 1991, **34**, pp 1067-1082.
44. HOSNI, M.H., COLEMAN, H.W., GARNER, J.W. and TAYLOR, R.P. Roughness element shape effects on heat transfer and skin friction in rough-wall turbulent boundary layers, *Int J Heat and Mass Tranfer*, 1993, **36**, pp 147-153.
45. ANDERSON, J.D. *Hypersonic and High Temperature Gas Dynamics*, 1998, McGraw-Hill Book Company (UK) Ltd. Maidenhead, UK.